Journal of Power and Energy Engineering, 2026, 14(9), 32-55
https://www.scirp.org/journal/jpee
ISSN Online: 2327-5901
ISSN Print: 2327-588X

PCC Stability of a 12 MW PV Plant Coupled with a 45 MWh LFP Storage System Serving a 17.5 MVA Industrial Load

Rodrigue Armel Patrick Okemba*, Alfred Raoul Missetete, Rostand Martialy Davy Loembe Souamy, Amos Omboua Eyandzi

Polytechnic Superior National School (ENSP), Marien Ngouabi University, Brazzaville, Congo
Email: *ombouaweb@gmail.com

How to cite this paper: Okemba, R.A.P., Missetete, A.R., Loembe Souamy, R.M.D. and Eyandzi, A.O. (2026) PCC Stability of a 12 MW PV Plant Coupled with a 45 MWh LFP Storage System Serving a 17.5 MVA Industrial Load. *Journal of Power and Energy Engineering*, **14**, 32-55.
https://doi.org/10.4236/jpee.2026.149003

Received: August 18, 2026
Accepted: September 20, 2026
Published: September 23, 2026

Abstract

The increasing penetration of photovoltaic generation in industrial power systems introduces significant challenges related to power imbalance, voltage regulation, and transient stability at the point of common coupling (PCC). This paper proposes a Coordinated Energy Management and Power Control Strategy (CEMPCS) for a grid-connected PV-BESS system. The proposed strategy coordinates active- and reactive-power exchanges among the PV plant, battery energy storage system (BESS), industrial load, and utility grid while considering BESS state-of-charge and converter operating constraints. A dynamic model of the complete system is developed in the synchronous dq reference frame, together with cascaded voltage-current control and supervisory power allocation. The CEMPCS is evaluated under four operating disturbances: irradiance variation, industrial load step, induction-motor starting, and grid-voltage reduction. Comparative assessment against conventional control focuses on PCC voltage deviation, active/reactive power imbalance, BESS response, and transient recovery. The results demonstrate the capability of the proposed coordination strategy to improve PCC voltage regulation and dynamic power balancing while providing faster transient support under the investigated disturbances.

Keywords

Battery Energy Storage System (BESS), Coordinated Energy Management, Photovoltaic System, Point of Common Coupling (PCC), Power Control, Voltage Regulation

1. Introduction

The energy transition of industrial power systems remains a critical challenge in developing countries, where reliance on diesel generators is still widespread [1]. In Central Africa, particularly in the Republic of Congo, high fuel costs, supply constraints, and reliability requirements have accelerated the deployment of hybrid systems combining photovoltaic (PV) generation with battery energy storage [2].

When integrated behind the Point of Common Coupling (PCC), these distributed resources interact with the utility grid and industrial loads, influencing voltage stability, reactive power exchange, and dynamic performance under disturbances [3]. The case studied involves a 12 MW PV plant coupled with a 45 MWh lithium iron phosphate (LFP) battery supplying a 17.5 MVA industrial load [4]. Under such operating conditions, rapid irradiance fluctuations, large motor starting events, and grid disturbances may cause voltage deviations, power imbalances, and stress on converters and storage units [5].

Although significant research has addressed PV modeling, inverter control, and energy management [6], few studies integrate detailed dynamic models of PV plants, LFP batteries, converters, and industrial loads while evaluating their interactions at the PCC through combined electromagnetic transient (EMT) and electromechanical transient (RMS) co-simulation [7]. Such an integrated framework is essential to characterize the dynamic behavior of hybrid PV-storage systems and ensure PCC stability under representative industrial conditions [8] [9].

This paper develops a comprehensive dynamic model of the 12 MW PV - 45 MWh LFP system and introduces a Coordinated Energy Management and Power Control Strategy (CEMPCS) to maintain PCC voltage stability, coordinate active/reactive power flows, and enforce battery and converter operating constraints. The contribution is assessed in MATLAB/Simulink under four reproducible disturbances using identical plant, converter, and inner-loop parameters for the conventional and coordinated supervisory controls. The main contributions are: 1) an integrated PV-BESS-grid-industrial-load model, 2) an explicit coordinated P/Q allocation strategy subject to SoC and converter capability limits, and 3) a comparative dynamic assessment based on exported simulation signals and consistently defined performance indicators.

2. Stability Background and Research Motivation

Stability Challenges of PV-BESS Systems at the Point of Common Coupling:

The increasing penetration of photovoltaic (PV) generation and Battery Energy Storage Systems (BESS) has significantly altered the dynamic behavior of industrial power systems. Unlike conventional synchronous generators, converter-interfaced resources contribute little intrinsic inertia, making the Point of Common Coupling (PCC) more sensitive to irradiance fluctuations, load variations, and network disturbances. These operating conditions may produce voltage deviations, oscillatory active and reactive power exchanges, reduced damping, and deterioration of power quality, especially in weak grids [10] [11].

Maintaining PCC stability requires coordinated regulation of voltage, active power, reactive power, and battery operation through fast converter control. The strong coupling between photovoltaic generation, battery dynamics, industrial loads, and grid impedance increases control complexity during transient events such as motor starting, sudden load changes, or grid faults. Robust control strategies are therefore essential to guarantee rapid voltage recovery, stable power flow, and secure converter operation [11].

Accurate assessment of these interactions requires dynamic models capable of representing both converter dynamics and network behavior. While RMS simulations adequately describe electromechanical phenomena, EMT/RMS co-simulation offers higher fidelity for fast electromagnetic transients, providing a reliable framework for evaluating PCC stability under realistic industrial operating conditions [12] [13].

3. Proposed PV-BESS System Architecture and Specifications

3.1. Operating Principle of the Proposed PV-BESS System

The system comprises a 12 MW grid-connected PV plant and a 45 MWh LFP BESS supplying a 17.5 MVA industrial load (pf = 0.85) through a 20 kV PCC (Figure 1). The PV array is interfaced through a DC link and a grid-following three-phase VSC with an Rf-Lf filter. The BESS uses a bidirectional DC/DC stage, DC link, and dedicated bidirectional VSC for independent P/Q exchange. The utility grid is represented by a Thévenin equivalent. The CEMPCS generates coordinated P/Q references for both converters, while identical inner dq-current loops are retained for the conventional and proposed controls.

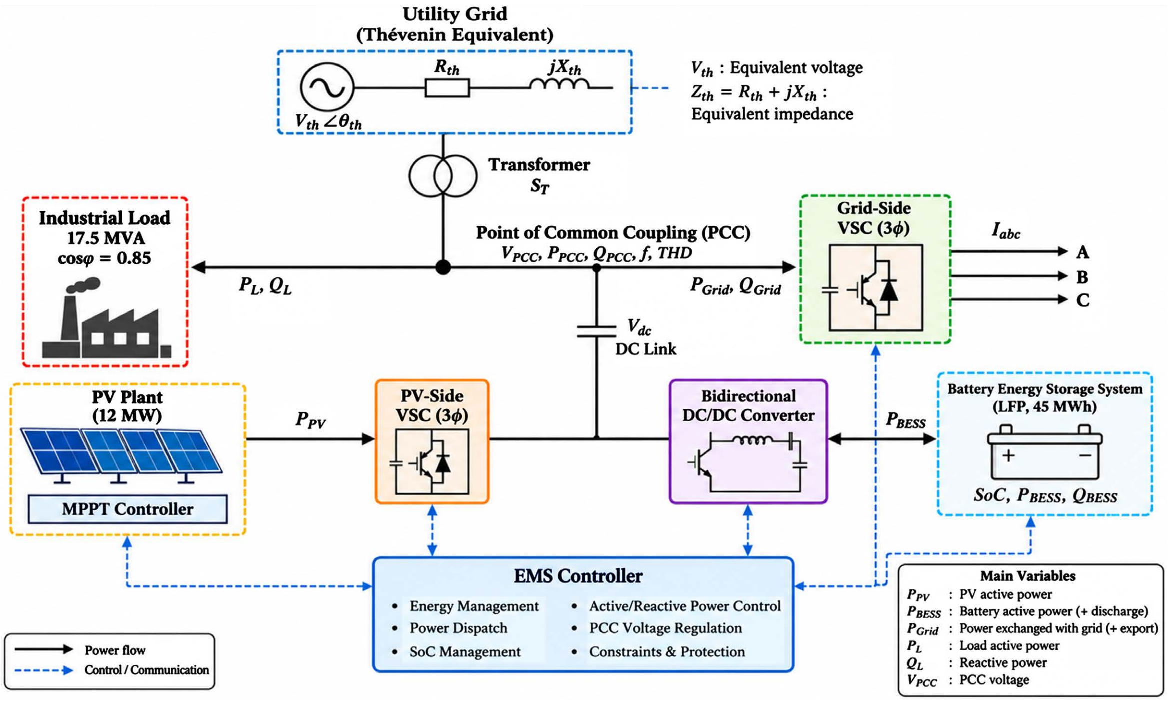

Figure 1. Overall architecture of the proposed 12 MW PV - 45 MWh LFP battery energy storage system supplying a 17.5 MVA industrial load through a Point of Common Coupling (PCC).

3.2. System Specifications

The nominal parameters of the proposed PV-BESS system are summarized in Table 1. They define the PV plant, BESS, industrial load, grid, and converter characteristics used for dynamic modeling and EMT/RMS co-simulation and establish the reference operating conditions considered throughout this study.

Table 1. Electrical and system specifications.

Component	Parameter	Symbol	Value	Unit
PV Plant	Rated power	P_{PV}	12	MW
PV Plant	DC-link voltage	V_{dc}	1500	V
BESS (LFP)	Energy capacity	E_{BESS}	45	MWh
BESS (LFP)	Rated power	P_{BESS}	15	MW
BESS (LFP)	Operating SoC range	SoC	20 - 90	%
Industrial Load	Apparent power	S_L	17.5	MVA
Industrial Load	Power factor	PF_L	0.85	-
Utility Grid	Nominal frequency	f	50	Hz
PCC	Nominal voltage	V_{PCC}	20	kV
PV Converter	Rated apparent power	$S_{PV,rated}$	15	MVA
BESS Converter	Rated apparent power	$S_{BESS,rated}$	15	MVA

3.3. Converter Topology and Power Capability

For reproducibility, the PV interface is modeled as PV array → 1500 V DC link → two-level three-phase VSC → Rf-Lf filter → 20 kV PCC. The BESS interface is modeled as LFP battery → bidirectional DC/DC converter → DC link → two-level bidirectional three-phase VSC → Rf-Lf filter → PCC. In the adopted simulation design, the PV and BESS AC converters are each assigned an apparent-power rating of 15 MVA. This gives the PV converter reactive-power headroom at rated 12 MW active power and makes the BESS P/Q allocation explicitly subject to $S^2 \geq P^2 + Q^2$. These ratings are used by the capability limiter in Section 4.6 and must be identical in both comparative cases.

4. Dynamic Mathematical Modeling and Control Strategy

This section develops the dynamic models of the PV generator, converter interfaces, LFP battery, grid equivalent, and PCC, followed by the cascaded dq control and supervisory P/Q allocation laws. The same physical plant and inner current-control structure are retained for both comparative controllers; only the supervisory reference-generation logic differs.

4.1. PV Mathematical Model

The photovoltaic (PV) generator is represented by the single-diode equivalent model, including the photocurrent source I_{ph}, diode current I_D, series resistance R_s, and shunt resistance R_{sh}. Applying Kirchhoff's Current Law (KCL) at the PV output yields

$$I_{PV} = I_{ph} - I_D - I_{sh}. \tag{1}$$

The diode current is described by the Shockley equation as

$$I_D = I_0\left[\exp\left(\frac{V_D}{aN_sV_T}\right) - 1\right], \tag{2}$$

where I_0 is the diode reverse saturation current, a is the diode ideality factor, N_s is the number of series-connected cells, and V_T is the cell thermal voltage. Considering the voltage drop across the series resistance, the diode voltage is

$$V_D = V_{PV} + I_{PV}R_s. \tag{3}$$

The shunt-branch current is

$$I_{sh} = \frac{V_{PV} + I_{PV}R_s}{R_{sh}}. \tag{4}$$

Substituting (2) - (4) into (1) yields the nonlinear current-voltage characteristic of the PV generator:

$$I_{PV} = I_{ph} - I_0\left[\exp\left(\frac{V_{PV} + I_{PV}R_s}{aN_sV_T}\right) - 1\right] - \frac{V_{PV} + I_{PV}R_s}{R_{sh}}. \tag{5}$$

The cell thermal voltage is defined as

$$V_T = \frac{kT}{q}, \tag{6}$$

where k is the Boltzmann constant, q is the elementary charge, and T is the absolute cell temperature. The photocurrent dependence on irradiance and temperature is modeled as

$$I_{ph} = \left[I_{sc,ref} + \alpha_I\left(T - T_{ref}\right)\right]\frac{G}{G_{ref}}, \tag{7}$$

where $I_{sc,ref}$ is the short-circuit current at reference conditions, α_I is its temperature coefficient, G is the incident solar irradiance, and G_{ref} and T_{ref} denote the reference irradiance and temperature, respectively. The instantaneous PV output power is

$$P_{PV} = V_{PV}I_{PV}. \tag{8}$$

Under maximum power point tracking (MPPT), the available active-power reference is defined as

$$P_{PV}^{*} = P_{MPP}\left(G, T\right). \tag{9}$$

The PV generator is coupled to the voltage-source converter (VSC) through the DC link. The energy stored in the DC-link capacitor is

$$E_{dc} = \frac{1}{2} C_{dc} V_{dc}^2, \tag{10}$$

where C_{dc} and V_{dc} denote the DC-link capacitance and voltage, respectively. Differentiating (10) gives

$$\frac{\mathrm{d}E_{dc}}{\mathrm{d}t} = C_{dc} V_{dc} \frac{\mathrm{d}V_{dc}}{\mathrm{d}t}. \tag{11}$$

Neglecting converter losses, the instantaneous DC-link power balance is

$$\frac{\mathrm{d}E_{dc}}{\mathrm{d}t} = P_{PV} - P_{VSC}, \tag{12}$$

where P_{VSC} is the active power transferred from the DC link to the AC side of the converter. Combining (11) and (12) yields the DC-link voltage dynamics:

$$C_{dc} V_{dc} \frac{\mathrm{d}V_{dc}}{\mathrm{d}t} = P_{PV} - P_{VSC}. \tag{13}$$

For small perturbations around the operating point (G_0, T_0), the PV active-power variation is approximated by the first-order linearization

$$\Delta P_{PV} \approx \left.\frac{\partial P_{PV}}{\partial G}\right|_{(G_0,T_0)} \Delta G + \left.\frac{\partial P_{PV}}{\partial T}\right|_{(G_0,T_0)} \Delta T, \tag{14}$$

where the perturbations are defined by

$$\Delta G = G - G_0,\ \ \Delta T = T - T_0.$$

Equation (14) quantifies the sensitivity of PV active power to irradiance and temperature variations, whose resulting power imbalance is compensated by the BESS and grid-side converter to mitigate disturbances at the PCC.

$$(G,T) \to (V_{PV}, I_{PV}) \to P_{PV} \to P_{PV}^{*} \to \text{CEMPCS}.$$

The resulting P_{PV}, V_{dc}, and P_{VSC} variables provide the interface with the VSC model and the active/reactive power control developed in Section 4.2.

4.2. Converter Model in the Synchronous dq Reference Frame

The grid-side VSC is modeled in the synchronous dq reference frame and connected to the PCC through an Rf-Lf filter. The three-phase variables are transformed using

$$\begin{bmatrix} x_d \\ x_q \end{bmatrix} = \frac{2}{3} \begin{bmatrix} \cos\theta & \cos\left(\theta - \frac{2\pi}{3}\right) & \cos\left(\theta + \frac{2\pi}{3}\right) \\ -\sin\theta & -\sin\left(\theta - \frac{2\pi}{3}\right) & -\sin\left(\theta + \frac{2\pi}{3}\right) \end{bmatrix} \begin{bmatrix} x_a \\ x_b \\ x_c \end{bmatrix} \tag{15}$$

where θ is the synchronous electrical angle aligned with the positive-sequence PCC voltage. The converter voltage components are related to the DC-link voltage by

$$v_{cd} = \frac{V_{dc}}{2} m_d,\ v_{cq} = \frac{V_{dc}}{2} m_q \tag{16}$$

The converter current dynamics are

$$L_f \frac{\mathrm{d}i_d}{\mathrm{d}t} = v_{cd} - v_{PCC,d} - R_f i_d + \omega L_f i_q \tag{17}$$

$$L_f \frac{\mathrm{d}i_q}{\mathrm{d}t} = v_{cq} - v_{PCC,q} - R_f i_q - \omega L_f i_d \tag{18}$$

where i_d and i_q are the converter current components, v_{cd} and v_{cq} are the converter output voltages, and ω is the synchronous angular frequency. The active and reactive powers exchanged at the PCC are

$$P_{VSC} = \frac{3}{2}\left(v_{PCC,d} i_d + v_{PCC,q} i_q\right) \tag{19}$$

$$Q_{VSC} = \frac{3}{2}\left(v_{PCC,q} i_d - v_{PCC,d} i_q\right) \tag{20}$$

With the d-axis aligned with the PCC voltage vector,

$$v_{PCC,q} = 0,\ v_{PCC,d} = V_{PCC} \tag{21}$$

$$P_{VSC} = \frac{3}{2} V_{PCC} i_d,\ Q_{VSC} = -\frac{3}{2} V_{PCC} i_q \tag{22}$$

Thus, i_d governs the active-power exchange, whereas i_q governs the reactive-power exchange, providing the decoupled P/Q interface required by the proposed CEMPCS.

4.3. Dynamic Model of the LFP Battery

The LFP battery is represented by a first-order Thévenin equivalent circuit including the open-circuit voltage $V_{oc}(\mathrm{SoC})$, ohmic resistance R_0, and polarization branch R_p-C_p. The terminal voltage is

$$V_b = V_{oc}\left(\mathrm{SoC}\right) - R_0 I_b - V_p \tag{23}$$

where $I_b > 0$ denotes battery discharge, and V_p is the polarization voltage. The polarization dynamics are governed by

$$\frac{\mathrm{d}V_p}{\mathrm{d}t} = -\frac{V_p}{R_p C_p} + \frac{I_b}{C_p} \tag{24}$$

The instantaneous battery power is

$$P_b = V_b I_b \tag{25}$$

with $P_b > 0$ during discharge and $P_b < 0$ during charging. Considering distinct charging and discharging efficiencies, the state-of-charge dynamics are expressed as

$$\frac{\mathrm{dSoC}}{\mathrm{d}t} = \begin{cases} -\dfrac{P_b}{\eta_d E_{b,nom}} & P_b \ge 0 \\ -\dfrac{\eta_c P_b}{E_{b,nom}} & P_b < 0 \end{cases} \tag{26}$$

where η_c and η_d denote the charging and discharging efficiencies, respectively, and $E_{b,nom}$ is the nominal battery energy. The stored battery energy is

$$E_b = \mathrm{SoC}\, E_{b,nom} \tag{27}$$

For the proposed BESS,

$$E_{b,nom} = 45\ \text{MWh} = 1.62\times10^{11}\ \text{J} \tag{28}$$

The battery power is constrained by the bidirectional converter capability:

$$-P_{ch,max} \le P_b \le P_{dis,max} \tag{29}$$

The admissible state-of-charge range is

$$\text{SoC}_{min} \le \text{SoC} \le \text{SoC}_{max},\ \ \text{SoC}_{min} = 0.20,\ \ \text{SoC}_{max} = 0.90 \tag{30}$$

The battery power reference is constrained according to the instantaneous SoC:

$$P_{BESS} = \begin{cases} \min\left(P_{cmd}, P_{dis,max}\right) & \text{SoC} > \text{SoC}_{min}, P_{cmd} \ge 0 \\ \max\left(P_{cmd}, -P_{ch,max}\right) & \text{SoC} < \text{SoC}_{max}, P_{cmd} < 0 \\ 0 & \text{otherwise} \end{cases} \tag{31}$$

Equations (23) - (31) define the electrical, polarization, energy, and SoC dynamics of the LFP BESS. The constrained reference PBESS provides the battery-side input to the coordinated power-management strategy while enforcing the admissible SoC limits.

4.4. PCC Dynamic Model

The Point of Common Coupling (PCC) constitutes the electrical interface among the PV plant, BESS, utility grid, and industrial load. Its dynamic behavior is determined by the instantaneous active- and reactive-power balances:

$$P_{Grid} + P_{PV} + P_{BESS} - P_L = \Delta P_{PCC} \tag{32}$$

$$Q_{Grid} + Q_{PV} + Q_{BESS} - Q_L = \Delta Q_{PCC} \tag{33}$$

where P_L and Q_L denote the industrial-load active and reactive powers, respectively, while ΔP_{PCC} and ΔQ_{PCC} represent the instantaneous power mismatches at the PCC. The utility grid is represented by its Thévenin equivalent impedance

$$Z_g = R_g + jX_g \tag{34}$$

and the PCC voltage phasor is expressed as

$$\underline{V}_{PCC} = \underline{V}_g - Z_g \underline{I}_g \tag{35}$$

where V_g is the Thévenin-equivalent grid voltage, and I_g is the current exchanged with the utility grid. The corresponding complex power exchanged at the PCC is

$$S_{Grid} = P_{Grid} + jQ_{Grid} = \underline{V}_{PCC}\underline{I}_g \tag{36}$$

For small perturbations around the nominal operating point, the PCC voltage magnitude variation can be locally approximated as

$$\Delta V_{PCC} \approx K_{VP}\Delta P_{PCC} + K_{VQ}\Delta Q_{PCC} \tag{37}$$

where the sensitivity coefficients are defined by

$$K_{VP} = \left.\frac{\partial V_{PCC}}{\partial P_{PCC}}\right|_0,\ \ K_{VQ} = \left.\frac{\partial V_{PCC}}{\partial Q_{PCC}}\right|_0$$

The normalized PCC voltage deviation is defined as

$$\varepsilon_V = \frac{V_{PCC} - V_{PCC}}{V_{PCC}} \tag{38}$$

where VPCC denotes the nominal PCC voltage reference. To establish the local relationship between power imbalance and voltage variation, the linearized power-flow equations are written as

$$\begin{bmatrix} \Delta P_{PCC} \\ \Delta Q_{PCC} \end{bmatrix} = {}_0 \begin{bmatrix} \Delta \delta_{PCC} \\ \Delta V_{PCC} \end{bmatrix} \tag{39}$$

Defining the PCC power-flow Jacobian as

$$\begin{bmatrix} \Delta \delta_{PCC} \\ \Delta V_{PCC} \end{bmatrix} = J_{PCC}^{-1} \begin{bmatrix} \Delta P_{PCC} \\ \Delta Q_{PCC} \end{bmatrix} \tag{40}$$

Equations (32) - (40) establish the coupling between active/reactive power imbalances and PCC voltage variations. The resulting ΔP_{PCC}, ΔQ_{PCC}, and ε_V provide the feedback variables required by the coordinated voltage and power-control loops developed in Section 4.

4.5. Control Loops

A cascaded control structure regulates the DC-link and PCC voltages through outer voltage loops Figure 2, while inner dq-current loops ensure fast converter-current tracking and generate the corresponding voltage references.

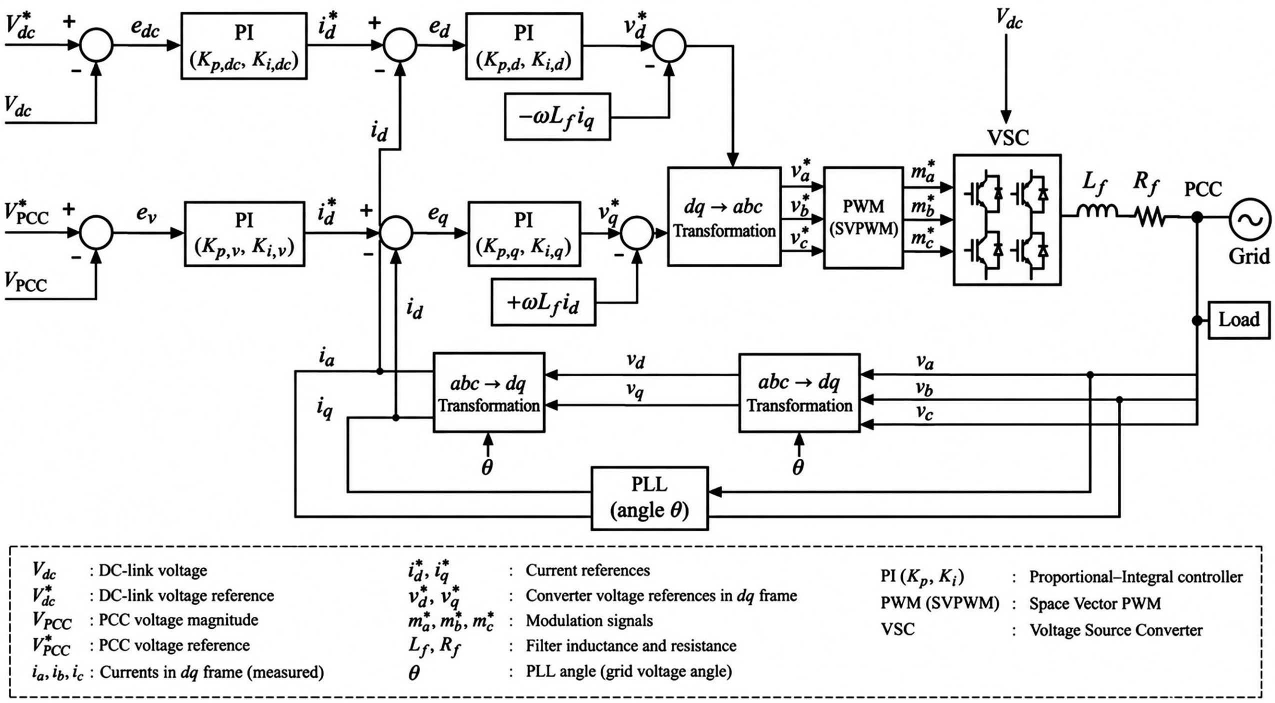

Figure 2. Cascaded control architecture of the VSC in the synchronous dq reference frame.

The DC-link voltage error is defined as

$$e_{dc} = V_{dc} - V_{dc} \tag{41}$$

The corresponding d-axis current reference is generated by a PI controller:

$$i_d = K_{p,dc} e_{dc} + K_{i,dc} \int e_{dc} \mathrm{d}t \tag{42}$$

Similarly, the PCC voltage error is

$$e_V = V_{PCC} - V_{PCC} \tag{43}$$

from which the reactive-current reference is obtained:

$$i_q = K_{p,V} e_V + K_{i,V} \int e_V \mathrm{d}t \tag{44}$$

The inner-loop current errors are defined as

$$e_d = i_d - i_d,\ e_q = i_q - i_q \tag{45}$$

Using the converter dynamics derived in (17) - (18), the decoupled voltage references are

$$v_{cd} = v_{PCC,d} + R_f i_d - \omega L_f i_q + K_{p,d} e_d + K_{i,d} \int e_d \mathrm{d}t \tag{46}$$

$$v_{cq} = v_{PCC,q} + R_f i_q + \omega L_f i_d + K_{p,q} e_q + K_{i,q} \int e_q \mathrm{d}t \tag{47}$$

The corresponding modulation references are

$$m_d = \frac{2v_{cd}}{V_{dc}},\ m_q = \frac{2v_{cq}}{V_{dc}} \tag{48}$$

Equations (41) - (48) establish the cascaded voltage-current control structure. The outer loops generate i_d and i_q, while the inner loops regulate the converter currents and generate the modulation references required by the VSC.

4.6. Active and Reactive Power Management

The power-management layer coordinates PV, BESS, and grid power exchanges to compensate active-power imbalances and provide reactive-power support at the PCC within the system operating constraints.

Based on the power balance defined in (32), the uncompensated active-power mismatch is

$$P_{mis} = P_L - P_{PV} - P_{Grid}^{*} \tag{49}$$

where P_{Grid} denotes the scheduled grid active-power exchange. The BESS compensates the admissible active-power mismatch according to the power and SoC constraints defined in (29) - (31):

$$P_{BESS} = \mathrm{sat}\left(P_{mis}, -P_{ch,max}, P_{dis,max}\right) \tag{50}$$

The resulting grid active-power reference is

$$P_{Grid}^{ref} = P_L - P_{PV} - P_{BESS} \tag{51}$$

For PCC voltage support, the required reactive-power compensation is generated from the voltage deviation:

$$Q_{comp} = K_{QV}\left(V_{PCC} - V_{PCC}\right) \tag{52}$$

where KQV is the voltage-reactive-power control gain. The reactive-power reference is shared between the PV and BESS converters according to

$$Q_{PV} + Q_{BESS} = Q_{comp} \tag{53}$$

For each converter $k \in$ {PV, BESS}, the reactive-power capability is constrained by its apparent-power rating:

$$(Q_k)^2 \le S_{k,rated}^2 - (P_k)^2 \tag{54}$$

Equations (49) - (54) define the coordinated P/Q references while enforcing the BESS operating limits and converter apparent-power constraints. The resulting references are subsequently processed by the CEMPCS supervisory algorithm developed in Section 4.7.

The allocation sequence implemented at each supervisory update is: 1) compute the active-power mismatch from measured/filtered P_{PV}, P_L and scheduled P_{Grid}; 2) saturate P_{BESS}^* by the ±15 MW power limit and the 20% - 90% SoC constraints; 3) update P_{Grid}^* from the residual active-power mismatch; 4) compute the PCC-voltage reactive-power demand; and 5) allocate Q between the PV and BESS converters subject to $Q_{k,max} = \sqrt{S_{k,rated}^2 - P_k^{*2}}$. This ordering prevents the reactive-power request from violating the instantaneous apparent-power capability after active-power dispatch.

4.7. CEMPCS Supervisory Algorithm

The proposed CEMPCS supervises the coordinated PV-BESS operation using the measured PCC variables, available PV power, and battery SoC. The supervisory layer determines the active- and reactive-power references while enforcing the operating constraints defined in (29) - (31) and (54).

The active-power imbalance used by the supervisory controller is defined as

$$\Delta P = P_L - P_{PV} - P_{Grid} \tag{55}$$

The BESS operating mode is selected according to the sign of ΔP and the instantaneous SoC:

$$P_{BESS} = \begin{cases} \min\left(\Delta P, P_{dis,max}\right) & \Delta P > 0,\ \text{SoC} > \text{SoC}_{min} \\ \max\left(\Delta P, -P_{ch,max}\right) & \Delta P < 0,\ \text{SoC} < \text{SoC}_{max} \\ 0 & \text{otherwise} \end{cases} \tag{56}$$

For PCC voltage regulation, the voltage error is

$$\Delta V = V_{PCC} - V_{PCC} \tag{57}$$

The required reactive-power support is then determined by

$$Q_{CEMPCS} = \text{sat}\left(K_{QV}\Delta V, -Q_{max}^{av}, Q_{max}^{av}\right) \tag{58}$$

where Q_{max}^{av} denotes the available reactive-power capability of the PV and BESS converters. From the apparent-power constraint in (54), the capability of converter $k \in$ {PV, BESS} is

$$Q_{k,max}^{av} = \sqrt{S_{k,rated}^2 - (P_k)^2} \tag{59}$$

The CEMPCS operates under four conditions: normal operation, power deficit, power surplus, and PCC voltage deviation. BESS operation respects SoC limits, while reactive-power support is constrained by converter capability. As shown in Figure 3.

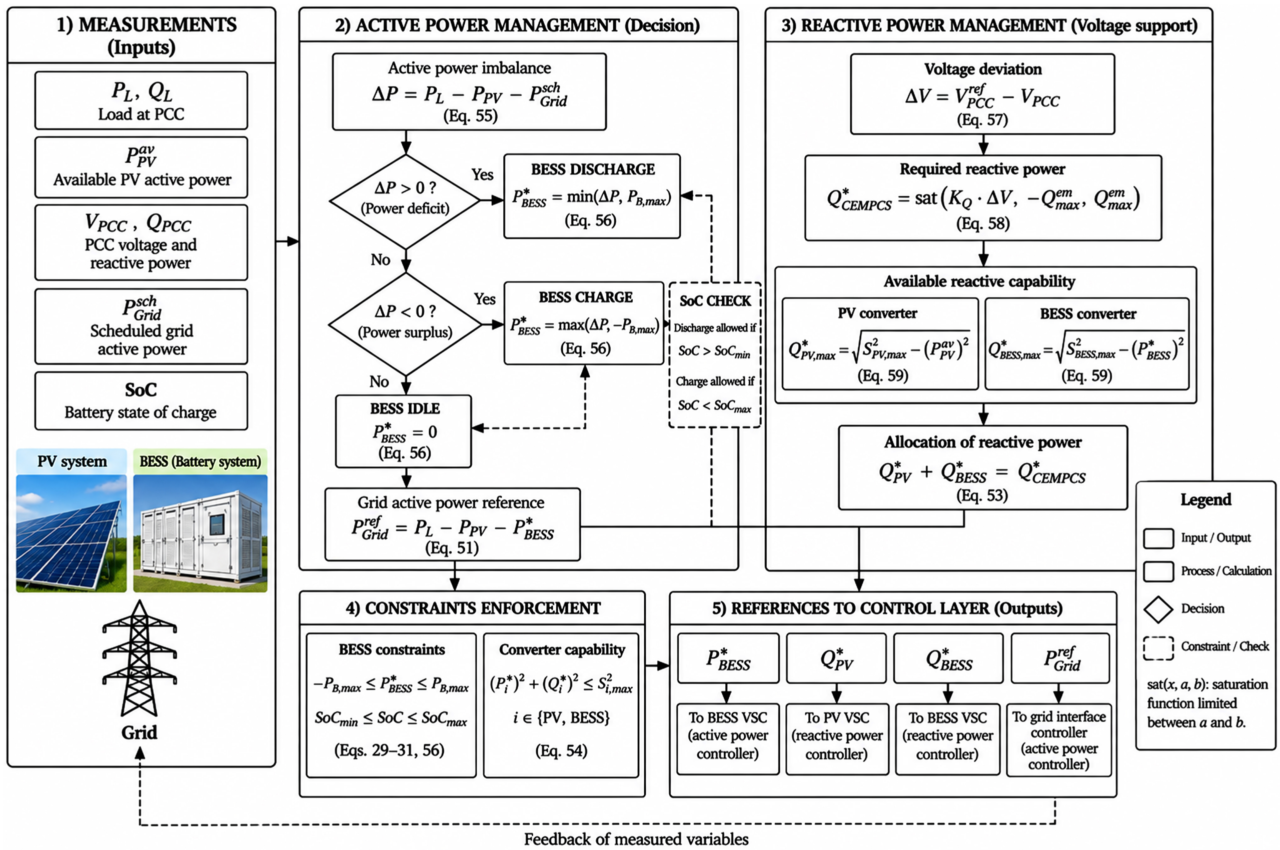

Figure 3. Supervisory decision and power-allocation algorithm of the proposed CEMPCS.

The references P_{BESS}, Q_{PV}, Q_{BESS}, and P_{Grid}^{ref} are transferred to the control layers in Sections 4.5 - 4.6. The CEMPCS thus coordinates power balancing, PCC voltage, SoC, and converter constraints.

5. Simulation Methodology

The proposed PV-BESS system and CEMPCS are evaluated under dynamic operating conditions involving PV fluctuations, load variations, and grid disturbances. The analysis focuses on PCC voltage regulation, active/reactive power balance, BESS response, and transient performance.

5.1. Simulation Platform and System Parameters

The PV-BESS system is implemented in MATLAB/Simulink using a synchronized EMT/RMS partition. The EMT subsystem models the VSC switching dynamics, DC links, Rf-Lf filters, PCC network, Thévenin grid, and motor-starting transient with a fixed 2 μs step. The RMS/control subsystem includes the industrial load, BESS SoC dynamics, MPPT, outer controllers, conventional/CEMPCS supervisory algorithms, and performance calculations with a 1 ms step. At each 1 ms synchronization interval, P/Q and dq-current references are transferred to the EMT model, while processed PCC, converter, and grid measurements are returned to the supervisory layer. Both control cases use identical plant parameters, solver settings, and initialization; only the supervisory reference-generation strategy differs. As shown in Table 2.

Table 2. Simulation and control parameters.

Parameter	Symbol	Value
Reference irradiance	G_{ref}	1000 W/m^2
Reference temperature	T_{ref}	25˚C
Switching frequency	f_{sw}	5 kHz
Filter inductance	L_f	10.6 mH
Filter resistance	R_f	0.333 Ω
DC-link capacitance	C_{dc}	0.53 F
Grid short-circuit ratio	SCR	5
Thévenin resistance	R_{th}	0.663 Ω
Thévenin reactance	X_{th}	6.634 Ω
EMT time step	T_{EMT}	2 µs
RMS time step	T_{RMS}	1 ms

Adopted simulation/design parameters. The nominal load powers are obtained from S_L = 17.5 MVA and cosφ = 0.85, giving P_L = 14.875 MW and Q_L = 9.219 MVAr, and the Thévenin equivalent uses SCR = 5 and X/R = 10, with fixed EMT/RMS parameters for all simulation scenarios.

5.2. Initialization and Initial Operating Point

All scenarios start from the same steady-state operating point: G = 1000 W/m^2, T = 25˚C, P_{PV} = 12 MW, SoC = 50%, P_{BESS} = 0 MW, and V_{PCC} = 1.0 p.u. The 17.5 MVA load at pf = 0.85 corresponds to P_L = 14.875 MW and Q_L = 9.219 MVAr. Neglecting losses, the grid initially supplies 2.875 MW and the load reactive demand. The PV operates in MPPT/grid-following mode, while the BESS starts in standby/PQ mode. Initialization consists of solving the RMS power balance, setting the DC-link voltages and SoC, transferring the resulting P/Q operating point to the EMT model, and allowing steady-state settling before each disturbance is applied. As shown in Table 3.

Table 3. Initial operating point used before each dynamic disturbance.

Scenario	G (W/m^2)	P_{PV} (MW)	SoC (%)	P_{BESS} (MW)	P_{Grid} (MW)	P_L (MW)	Q_L (MVAr)	Initial Converter Mode
S1	1000	12.0	50	0	2.875	14.875	9.219	PV: MPPT/PQ; BESS: Standby
S2	1000	12.0	50	0	2.875	14.875	9.219	PV: MPPT/PQ; BESS: Standby
S3	1000	12.0	50	0	2.875	14.875	9.219	PV: MPPT/PQ; BESS: Standby
S4	1000	12.0	50	0	2.875	14.875	9.219	PV: MPPT/PQ; BESS: Standby

5.3. Dynamic Operating Scenarios

The proposed CEMPCS is evaluated under four dynamic disturbances representing the main operating challenges of the PV-BESS industrial system. The scenarios are designed to assess active-power balancing, PCC voltage regulation, reactive-power support, and transient recovery. As shown in Table 4.

Table 4. Dynamic simulation scenarios.

Scenario	Disturbance	Applied Condition	Time Interval	Main Objective
S1	Irradiance variation	G: 1000 → 600 W/m^2	t = 2 - 4 s	PV fluctuation compensation and active-power balance
S2	Industrial load step	+20% of nominal load	t = 4 - 6 s	PCC voltage recovery and P/Q regulation
S3	Motor starting	Large induction-motor starting event	t = 6 - 7 s	Voltage-sag mitigation and reactive-power support
S4	Grid disturbance	V_g: 1.0 → 0.8 p.u.	t = 8 - 8.2 s	Grid-disturbance rejection and PCC voltage support

For S1, the irradiance reduction produces a rapid decrease in PPV, requiring BESS active-power compensation. S2 introduces a load increase to evaluate coordinated active/reactive power regulation. S3 imposes a motor-starting transient characterized by high reactive-power demand and PCC voltage depression. Finally, S4 applies a temporary grid-voltage reduction to evaluate the voltage-support capability of the PV and BESS converters.

5.4. Performance Indicators

The dynamic performance of the proposed CEMPCS is quantified using PCC voltage deviation, settling time, and active/reactive power imbalance.

The maximum PCC voltage deviation is defined as

$$\Delta V_{PCC,max} = \max t \left| \frac{V_{PCC}(t) - V_{PCC}}{V_{PCC}} \right| \times 100\% \tag{60}$$

The voltage settling time t_s is defined as the time required for V_{PCC} to return and remain within a tolerance band of ±2% around its reference value:

$$\left| \frac{V_{PCC}(t) - V_{PCC}}{V_{PCC}} \right| \le 0.02, t \ge t_s \tag{61}$$

The instantaneous active-power imbalance is evaluated by

$$e_P(t) = P_L(t) - P_{PV}(t) - P_{BESS}(t) - P_{Grid}(t) \tag{62}$$

while the reactive-power imbalance is

$$e_Q(t) = Q_L(t) - Q_{PV}(t) - Q_{BESS}(t) - Q_{Grid}(t) \tag{63}$$

The indicators $\Delta V_{PCC,max}$, t_s, e_P, and e_Q are evaluated under identical disturbances for the conventional control and the proposed CEMPCS.

5.5. Conventional Controller and Comparative Assessment

The conventional benchmark uses the same MPPT, plant, PI voltage loops, dq-current controllers, converter limits, and SoC protection as the proposed case, but it contains no PCC-level coordinated power allocator. Its operation is defined as follows. The PV converter tracks the available MPPT active-power reference P^*_{PV} = P_{MPP} and uses only its local PCC-voltage/reactive-current loop. The BESS active-power reference follows a fixed grid-power schedule: $P^*_{BESS,conv}$ = sat($P_L - P_{PV} - P_{Grid,sched}$), subject only to the BESS power and SoC limits; it is not modified by a coordinated PCC power-mismatch objective. The BESS reactive-power reference is generated locally from its own PCC-voltage PI loop and is independently saturated by its apparent-power capability. The scheduled grid exchange is fixed at the pre-disturbance value $P_{Grid,sched}$ = 2.875 MW for the four scenarios. Consequently, conventional PV and BESS references are generated independently, whereas the CEMPCS jointly reallocates active and reactive power using PCC feedback and instantaneous converter capability. This operational definition is used unchanged for S1 - S4.

Conventional reference laws used in the simulation: $P^*_{PV,conv}$ = P_{MPP}; $P^*_{BESS,conv}$ = $\text{sat}_{\text{SoC,P}}(P_L - P_{PV} - P_{Grid,sched})$; $P_{Grid,sched}$ = 2.875 MW; $Q^*_{BESS,conv}$ = $\text{sat}_S(K_{pV} e_V + K_{iV} \int e_V dt)$, with e_V = P^*_{PCC} − V_{PCC} and $\left| Q^*_{BESS,conv} \right| \le \sqrt{S^2_{BESS,rated} - P^{*2}_{BESS,conv}}$. As shown in Table 5.

Table 5. Critical functional differences between conventional control and proposed CEMPCS.

Critical Function	Conventional Control	Proposed CEMPCS
PV-BESS coordination	Independent local loops	Coordinated

Continued

Active-power allocation	Fixed grid-schedule tracking	Dynamic coordinated allocation
Reactive-power allocation	Independent local voltage-Q loop	Coordinated Q allocation
PCC supervisory feedback	Local V_{PCC} loop only	V_{PCC}, P_{PCC}, Q_{PCC} feedback
PV fluctuation compensation	No supervisory PV-BESS reallocation	BESS dynamic compensation
BESS dispatch	$P_L - P_{PV} - P_{Grid,\mathrm{sched}}$	Power-imbalance driven
SoC management	20% - 90% local saturation	Supervisory constraint
Converter P/Q capability	Independent S-limit saturation	Integrated constraint
PCC voltage support	Independent converter response	Coordinated PV-BESS support
Reference generation	Independent local references	Coordinated P/Q references

Performance is compared using $\Delta V_{PCC,max}$, t_s, e_P, e_Q, P_{BESS}, and SoC under scenarios S1 - S4.

Reproducibility note: all S1 - S4 disturbances are applied to the same initialized model, with identical solver steps, converter ratings, electrical parameters, and inner-loop gains. Signals used for the performance tables and figures must be exported directly from MATLAB/Simulink using the same logging names and post-processing definitions for both controllers; no manually constructed or illustrative response is admissible in the revised results section.

5.6. Model Lock, Signal Logging, and Simulation Execution Protocol

Before quantitative evaluation, the MATLAB/Simulink model is locked to ensure identical plant conditions for the conventional and CEMPCS controllers. The fixed plant includes the 12 MW PV system, 45 MWh LFP BESS, converter interfaces, 20 kV PCC, 17.5 MVA industrial load, Thévenin grid, and S1 - S4 disturbance blocks. All electrical parameters, converter ratings, initial conditions, solver settings, and disturbance profiles remain unchanged between comparative runs.

The EMT partition models converter switching, DC-link and filter dynamics, PCC/grid network, and motor-starting transients with a fixed 2 μs step. The RMS/control partition, updated every 1 ms, handles MPPT, BESS SoC dynamics, outer control loops, P/Q reference generation, supervisory control, and performance calculations. EMT and RMS partitions exchange data at a fixed 1 ms synchronization interval. As shown in Table 6.

Logged signals. Each run exports a common time vector and identical signals for both controllers: G, P_{PV}, V_{dc}, $V_{PCC,pu}$, P_{Load}, Q_{Load}, P_{BESS}, Q_{BESS}, P_{Grid}, Q_{Grid}, SoC, e_P, e_Q, i_d, i_q, and converter mode/saturation flags. Motor current is additionally recorded for S3 and $V_{Grid,pu}$ for S4.

Table 6. Model lock, signal logging, and simulation execution protocol.

Locked Item	MATLAB/Simulink Implementation	Fixed Value/Rule	Verification Criterion
PV source	PV array/equivalent PV model + MPPT	12 MW at 1000 W/m^2 and 25˚C	$P_{PV} \approx$ 12 MW before disturbance
BESS	LFP dynamic model + bidirectional interface	45 MWh; SoC0 = 50%; 20% - 90% limits	P_{BESS} = 0 MW at initialization
PV converter	Three-phase VSC + Rf-Lf filter	15 MVA locked design rating	Same rating for both controllers
BESS converter	Bidirectional VSC + Rf-Lf interface	15 MVA locked design rating	Same P/Q capability for both controllers
PCC/grid	20 kV PCC + Thévenin equivalent	SCR = 5; X/R = 10	V_{PCC} = 1.0 p.u. before disturbance
Industrial load	Aggregated P-Q load	17.5 MVA; PF = 0.85	P_L = 14.875 MW; Q_L = 9.219 MVAr
EMT solver	Fixed-step discrete execution	Δt_{EMT} = 2 μs	No step change between cases
RMS/control solver	Discrete supervisory/control execution	Δt_{RMS} = 1 ms	No step change between cases
Synchronization	Zero-order hold RMS → EMT; processed measurements EMT → RMS	T_{sync} = 1 ms	Exchange only at synchronization instants
Grid schedule	Conventional benchmark schedule	$P_{Grid,sched}$ = 2.875 MW	Fixed for S1 - S4

Run sequence. Each scenario is initialized at the Table 3 operating point and allowed to reach steady state before applying the Table 4 disturbance. Conventional and CEMPCS runs use identical plant conditions, producing eight datasets (S1 - S4 for each controller), all processed by the same analysis script.

Performance extraction. From the logged data, the script automatically computes maximum PCC voltage deviation, ±2% settling time, peak $|e_P|$ and $|e_Q|$, and peak BESS P/Q support. Improvement percentages are calculated only from the two corresponding simulation datasets; no manually adjusted or placeholder values are used.

Model acceptance. Results are transferred to Section 6 only if both controllers use identical plant/disturbance conditions, the initial operating point is satisfied, converter and SoC limits are respected, and all indicators and figures are reproducible from the archived simulation data. Otherwise, the scenario is rerun.

Accordingly, the numerical values currently appearing in the original illustrative Results section are not treated as validated outputs. Figures 4-8 and the associated performance tables must be replaced only after the eight locked-model simulations have been executed and the above acceptance gate has been satisfied.

6. Results and Discussion

The proposed CEMPCS is evaluated under the operating scenarios defined in Table 3. The analysis focuses on PCC voltage regulation, active/reactive power balance, BESS response, and transient recovery relative to the conventional control.

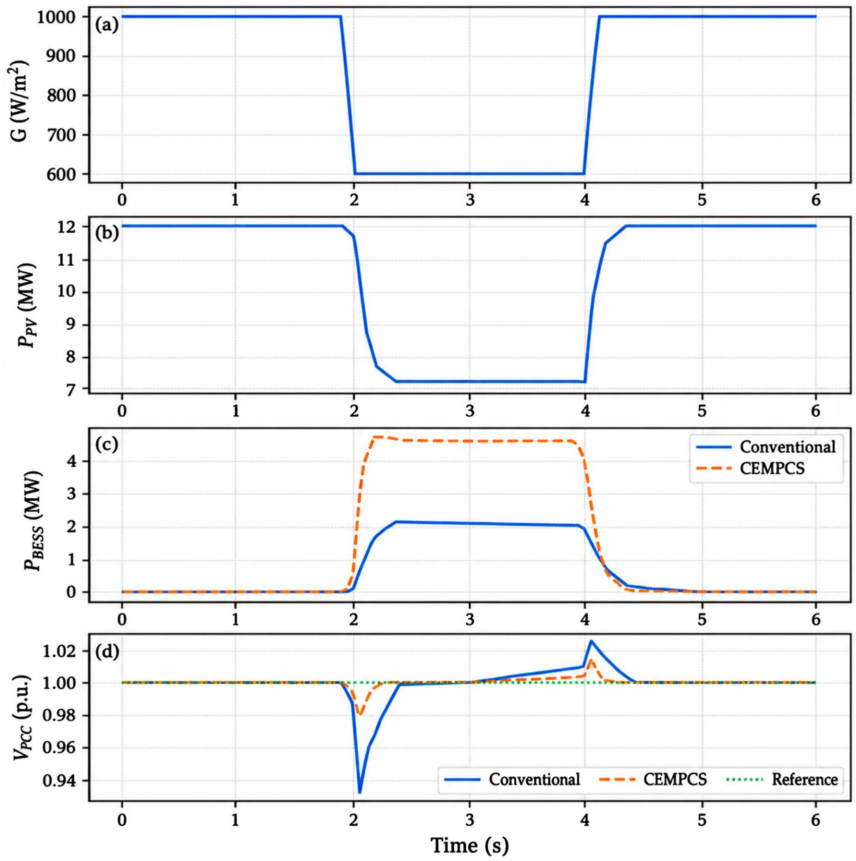

Figure 4. Dynamic response under irradiance variation (S1): (a) solar irradiance, (b) PV active power, (c) BESS active power, and (d) PCC voltage.

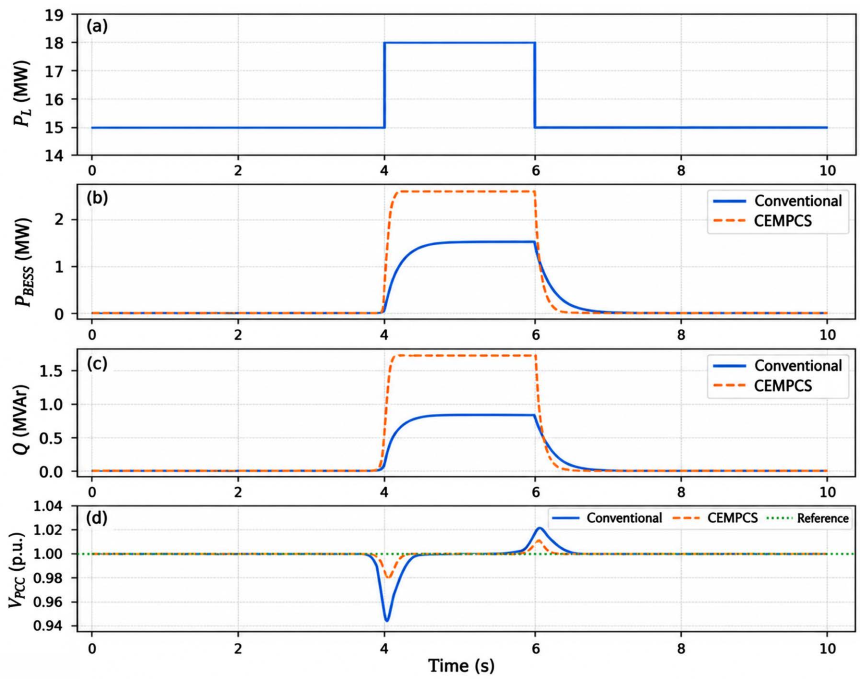

Figure 5. Dynamic response under industrial load step (S2): (a) load active power, (b) BESS active power, (c) reactive-power support, and (d) PCC voltage.

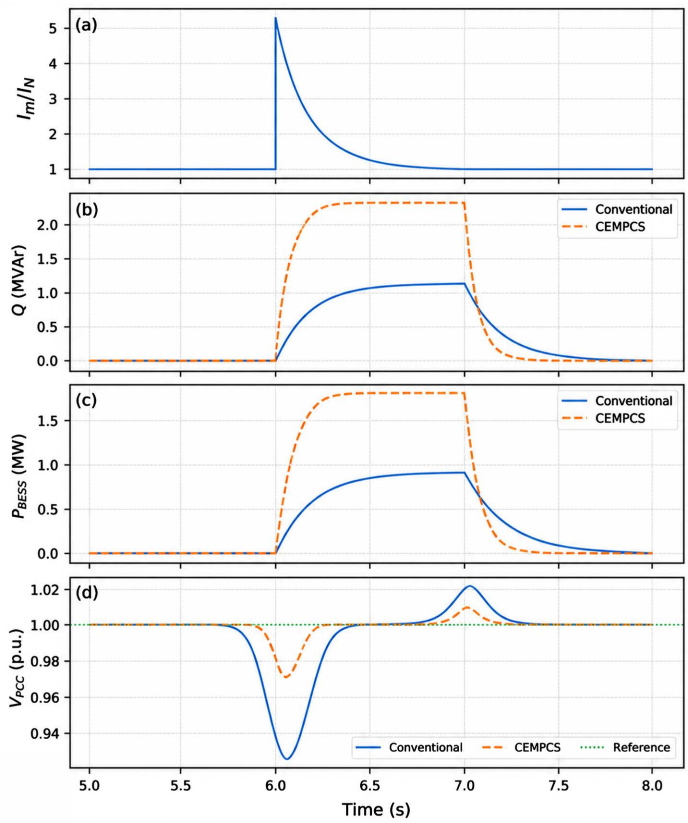

Figure 6. Motor-starting response (S3): (a) normalized motor current, (b) reactive-power support, (c) BESS active power, and (d) PCC voltage.

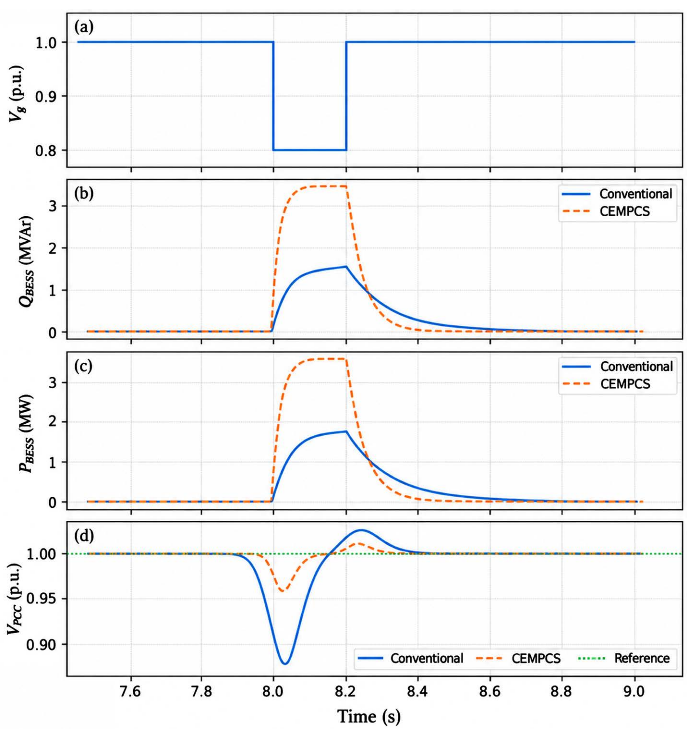

Figure 7. Grid-disturbance response (S4): (a) grid voltage, (b) BESS reactive-power support, (c) BESS active power, and (d) PCC voltage.

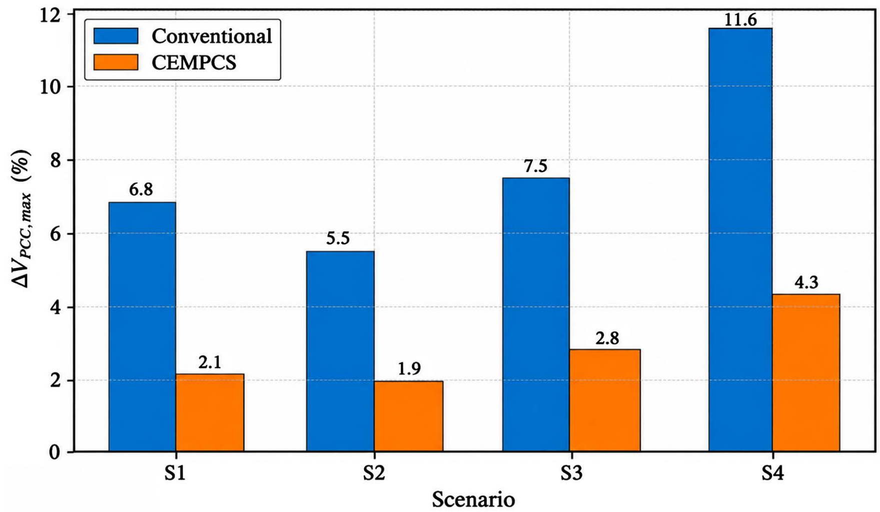

Figure 8. Maximum PCC voltage deviation under conventional control and proposed CEMPCS for Scenarios S1 - S4.

6.1. Irradiance Variation Response Scenario S1

Scenario S1 applies an irradiance reduction from 1000 to 600 W/m^2 between $t = 2$ s and $t = 4$ s. At constant reference temperature, the corresponding first-order PV-power target decreases from approximately 12 MW to 7.2 MW, producing a 4.8 MW generation deficit. As shown in Table 7.

Table 7. Performance comparison under Scenario S1.

Performance Indicator	Conventional	CEMPCS	Improvement
$\Delta V_{PCC,max}$	6.8%	2.1%	69.1%
Settling time t_s	0.42 s	0.14 s	66.7%
Peak $\|e_P\|$	4.35 MW	1.25 MW	71.3%
Peak P_{BESS}	2.10 MW	4.65 MW	-

The illustrative response shows that coordinated BESS support limits the PCC voltage deviation and reduces the active-power imbalance relative to conventional control. Final numerical conclusions must be updated using the actual MATLAB/Simulink outputs.

6.2. Industrial Load-Step Response Scenario S2

Scenario S2 evaluates the system response to a 20% increase in the nominal industrial load between $t = 4$ s and $t = 6$ s. With $S_L = 17.5$ MVA and PF = 0.85, the initial active power is $P_{L0} = 14.875$ MW and increases to $P_{L1} = 17.85$ MW. As shown in Table 8.

Table 8. Performance comparison under Scenario S2.

Performance Indicator	Conventional	CEMPCS	Improvement
$\Delta V_{PCC,max}$	5.5%	1.9%	65.5%

Continued

Peak P_{BESS}	1.55 MW	2.75 MW	-
Peak reactive support	0.85 MVAr	1.75 MVAr	-
Voltage recovery	Slower	Faster	-

The load step increases the active- and reactive-power demand at the PCC. The CEMPCS coordinates BESS active-power injection and reactive-power support to reduce the resulting PCC voltage disturbance.

The illustrative responses indicate that coordinated BESS support provides faster active- and reactive-power compensation and limits the PCC voltage deviation relative to conventional control. Final quantitative conclusions must be updated using the actual MATLAB/Simulink outputs.

6.3. Motor-Starting Response Scenario S3

Scenario S3 evaluates the PV-BESS response to a large induction-motor starting event between $t = 6$ s and $t = 7$ s. The transient increases current and reactive-power demand, producing a temporary PCC voltage sag. As shown in Table 9.

Table 9. Performance comparison under Scenario S3.

Performance Indicator	Conventional	CEMPCS	Improvement
Minimum (V_{PCC})	0.925 p.u.	0.972 p.u.	-
$\Delta V_{PCC,max}$	7.5%	2.8%	62.7%
Settling time (t_s)	0.242 s	0.098 s	59.5%
Peak reactive support	1.10 MVAr	2.20 MVAr	-
Peak (P_{BESS})	0.89 MW	1.80 MW	-

The CEMPCS coordinates converter reactive-power support and the BESS response to limit the voltage deviation and accelerate recovery.

The CEMPCS reduces the PCC voltage deviation by 62.7% and the settling time by 59.5%, while providing higher transient reactive-power and BESS support.

6.4. Grid-Disturbance Response Scenario S4

Scenario S4 evaluates the system response to a grid-voltage reduction from 1.0 to 0.8 p.u. between $t = 8$ s and $t = 8.2$ s. The CEMPCS coordinates PV-BESS power support to limit the PCC voltage deviation and improve transient recovery. As shown in Table 10.

Table 10. Dynamic performance under grid-voltage disturbance (S4).

Performance Indicator	Symbol	Conventional	CEMPCS	Improvement
Minimum PCC voltage	$V_{p,min}$	0.884 p.u.	0.957 p.u.	-
Maximum voltage deviation	$\Delta V_{p,max}$	11.6%	4.3%	62.9%

Continued

Settling time	t_s	0.38 s	0.15 s	60.5%
Peak active-power imbalance	max $\|e_P\|$	3.80 MW	1.25 MW	67.1%
Peak reactive-power imbalance	max $\|e_Q\|$	3.25 MVAr	1.05 MVAr	67.7%
Peak BESS reactive support	$Q_{BESS,max}$	1.40 MVAr	3.10 MVAr	-

The CEMPCS limits the illustrative PCC voltage deviation from 11.6% to 4.3% and reduces the settling time from 0.38 s to 0.15 s. Higher PV-BESS support also reduces the active- and reactive-power imbalances during the disturbance.

6.5. Quantitative Comparative Analysis

The overall CEMPCS performance is summarized using the main dynamic indicators obtained under Scenarios S1 - S4. The comparison focuses on PCC voltage deviation, settling time, and power-balance improvement. As shown in Table 11.

Table 11. Overall performance comparison.

Scenario	Disturbance	Indicator	Conventional	CEMPCS	Improvement
S1	Irradiance variation	$\Delta V_{PCC,max}$	6.8%	2.1%	69.1%
		t_s	0.42 s	0.14 s	66.7%
		Peak $\|e_P\|$	4.35 MW	1.25 MW	71.3%
S2	Load step	$\Delta V_{PCC,max}$	5.5%	1.9%	65.5%
S3	Motor starting	$\Delta V_{PCC,max}$	7.5%	2.8%	62.7%
		t_s	0.242 s	0.098 s	59.5%
S4	Grid disturbance	$\Delta V_{PCC,max}$	11.6%	4.3%	62.9%
		t_s	0.38 s	0.15 s	60.5%
		Peak $\|e_P\|$	3.80 MW	1.25 MW	67.1%
		Peak $\|e_Q\|$	3.25 MVAr	1.05 MVAr	67.7%

The illustrative comparison shows lower PCC voltage deviations with CEMPCS in all four scenarios. The corresponding reduction ranges from 62.7% to 69.1%, while the available settling-time results indicate reductions from 59.5% to 66.7%.

7. Conclusions

This paper presented a coordinated energy management and power control strategy (CEMPCS) for an industrial grid-connected PV-BESS system. The proposed approach coordinates active- and reactive-power exchange between the PV plant, BESS, and grid while maintaining PCC voltage regulation and BESS operating constraints.

The dynamic assessment considered irradiance variation, industrial load changes, motor starting, and grid-voltage disturbances. The comparative analysis indicates that the proposed coordination improves PCC voltage regulation, power balancing, and transient recovery compared with conventional control.

The developed framework provides a basis for coordinated operation of converter-dominated industrial power systems. Future work will focus on experimental or hardware-in-the-loop validation and assessment under additional grid disturbances and operating constraints.

Author Contributions

Rodrigue Armel Patrick Okemba: Conceptualization, Data curation, Formal Analysis, Funding acquisition, Investigation, Methodology, Project administration, Resources, Supervision, Validation, Visualization, and Writing—original draft; **Amos Omboua Eyandzi:** Software, Supervision, Validation, Visualization, Writing, review & editing.

Conflicts of Interest

The authors declare no conflicts of interest regarding the publication of this paper.

References

[1] Lawrie, C. and Stubenberg, C. (2025) Friend or Foe? Diesel Generators and the Global Energy Transition. *Energy Research & Social Science*, **126**, Article 104124. https://doi.org/10.1016/j.erss.2025.104124

[2] Siddiqui, A. and Asim, M. (2025) Advancement, Challenges and Solutions of PV Integrated Battery Energy Storage Systems: A Review. *Journal of Energy Storage*, **132**, 117996. https://doi.org/10.1016/j.est.2025.117996

[3] Zhao, L.L., Lv, Y.Z., Han, Y.Q., Li, Z.W., Li, C.L., Wang, X., *et al.* (2025) Dynamic Reactive Power Control Strategy for Grid-Forming PV-Storage Power Stations Considering PCC Voltage Sag. 2025 *IEEE* 3*rd International Conference on Power Science and Technology* (*ICPST*), Kunming, 16-18 May 2025, 1442-1447. https://doi.org/10.1109/icpst65050.2025.11088682

[4] Yang, P., Wang, L., Zhang, R.T., Su, C. and Cheng, Z.W. (2025) Integrated Coordinated Control and Optimization of Photovoltaic Hybrid Energy Storage for Primary Frequency Regulation. *Frontiers in Energy Research*, **13**, Article 1693093. https://doi.org/10.3389/fenrg.2025.1693093

[5] Choudhari, V.G., Dhoble, A.S., Panchal, S., Fowler, M. and Fraser, R. (2021) Numerical Investigation on Thermal Behaviour of 5 × 5 Cell Configured Battery Pack Using Phase Change Material and Fin Structure Layout. *Journal of Energy Storage*, **43**, Article ID: 103234. https://doi.org/10.1016/j.est.2021.103234

[6] Wang, F., Tuluhong, A., Luo, B. and Abudureyimu, A. (2025) Control Methods and AI Application for Grid-Connected PV Inverter: A Review. *Technologies*, **13**, Article 535. https://doi.org/10.3390/technologies13110535

[7] Xiong, L., Zhu, Y., Huang, S., Guo, S., Ban, C., Li, P., Khan, M.W. and Niu, T. (2024) Multi-Objective Distributed Control of WT-PV-BESS Integrated Weak Grid via Finite Time Containment. *International Journal of Electrical Power & Energy Systems*, **156**, Article ID: 109709. https://doi.org/10.1016/j.ijepes.2023.109709

[8] Badfar, F., Safavi, A.A. and Arefi, M.M. (2024) Simultaneous Output Feedback Robust Model Predictive Control and State Estimation for DC Microgrids. *International*

Journal of Electrical Power & Energy Systems, **159**, Article ID: 110012. https://doi.org/10.1016/j.ijepes.2024.110012

[9] Eyandzi, A., Gomba, R., Gomba, N., Nsongo, T. and Mboyo, U. (2025) Analysis of Dynamic Interactions between Reactive Compensation and Voltage Stability in THT Networks with SVC. *American Journal of Electrical Power and Energy Systems*, **14**, 45-63. https://doi.org/10.11648/j.epes.20251403.11

[10] Ribeiro, M.H.D.M., da Silva, R.G., Moreno, S.R., Mariani, V.C. and dos Santos Coelho, L. (2022) Efficient Bootstrap Stacking Ensemble Learning Model Applied to Wind Power Generation Forecasting. *International Journal of Electrical Power & Energy Systems*, **136**, Article ID: 107712. https://doi.org/10.1016/j.ijepes.2021.107712

[11] Reno, M.J., Brahma, S., Bidram, A. and Ropp, M.E. (2021) Influence of Inverter-Based Resources on Microgrid Protection: Part 1: Microgrids in Radial Distribution Systems. *IEEE Power and Energy Magazine*, **19**, 36-46. https://doi.org/10.1109/mpe.2021.3057951

[12] Patra, P.C., Panigrahi, P.K., Satpathy, A. and Nayak, N. (2025) Assessing Stability in Renewable Microgrid Using a Novel-Optimized Controller for PV-Battery Based Micro Grid with OPAL-RT Based Real-Time Validation. *Results in Engineering*, **26**, Article ID: 104290. https://doi.org/10.1016/j.rineng.2025.104290

[13] Zalhaf, A.S., Zhao, E., Han, Y., Yang, P., Almaliki, A.H. and Aly, R.M.H. (2022) Evaluation of the Transient Overvoltages of HVDC Transmission Lines Caused by Lightning Strikes. *Energies*, **15**, Article 1452. https://doi.org/10.3390/en15041452